Two-dimensional spectroscopy: An approach to distinguish Förster and Dexter transfer processes in coupled nanostructures

Judith F. Specht, Andreas Knorr, and Marten Richter*

Institut für Theoretische Physik, Nichtlineare Optik und Quantenelektronik, Technische Universität Berlin, Hardenbergstr. 36, EW 7-1, 10623 Berlin, Germany

(Received 10 November 2014; revised manuscript received 8 April 2015; published 29 April 2015)

The linear and two-dimensional coherent optical spectra of Coulomb-coupled quantum emitters are discussed with respect to the underlying coupling processes. We present a theoretical analysis of the two different resonance energy transfer mechanisms between coupled nanostructures: Förster and Dexter interaction. Our investigation shows that the features visible in optical spectra of coupled quantum dots can be traced back to the nature of the underlying coupling mechanism (Förster or Dexter). Therefore, we discuss how the excitation transfer pathways can be controlled by choosing particular laser polarizations and mutual orientations of the quantum emitters in coherent two-dimensional spectroscopy. In this context, we analyze to what extent the delocalized double-excitonic states are bound to the optical selection rules of the uncoupled system.

DOI: 10.1103/PhysRevB.91.155313 PACS number(s): 78.40.Fy, 78.47.jh, 78.67.Hc

I. INTRODUCTION

Within the last years, the development of precise and highly efficient crystal growth techniques has given rise to the fabrication of high-performance semiconductor devices with tunable optoelectronic and transport properties. Quantum confined nanostructures such as semiconductor quantum dots are used in various applications such as quantum dot lasers [1], single-photon sources [2], light-emitting diodes [3], and solar cells [4]. In particular, a detailed, quantitative understanding of the exciton dynamics in coupled nanostructures driven by coherent, ultrafast laser pulses is of great interest for quantum information [5]. The electronic properties and optical spectra of such coupled quantum systems can be considerably affected by Coulomb interaction processes induced by optically generated electron-hole pairs [6–8].

Therefore, investigating the Coulomb induced resonance energy transfer mechanisms between two nanostructures has been a central topic of research. There have been several experimental [9–11] and theoretical studies [12–15] on the spectroscopic signatures of Förster (dipole-dipole) excitation transfer between colloidal and self-assembled quantum dots. In this paper, we also consider direct electronic exciton transfer, i.e., the Dexter mechanisms [16], and include different spin states of the interacting electrons. *Our goal is to work out specific signatures of Förster and Dexter transfer in optical spectra of coupled semiconductor quantum dots:* Dexter transfer describes a direct exchange of electrons between the nanostructures and thus requires an electronic wave-function overlap. The spin of the transferred electron is conserved in the case of Dexter coupling. In contrast, Förster coupling denotes a dipole-dipole–type interaction which can either transfer or flip the spin state of the transferred exciton in quantum dot structures [17]. Since Förster coupling elements depend on the microscopic interband dipole orientations, spin-preserving and spin-flipping Förster coupling strengths can be manipulated by changing the mutual orientation of the two nanostructures [17]. This offers the opportunity to control quantum information with respect to the spin state of the transferred exciton, which is of particular interest for future quantum computational applications based on the electron spin [18,19].

Both Förster and Dexter coupling processes induce an excitation energy transfer from an initially excited donor to an acceptor [16,20–22]. This causes a hybridization of the excited states of the individual quantum emitters into new excitonic states potentially delocalized over the hybrid system. The characteristic optical resonances of the delocalized single-exciton states are encoded in linear absorption spectra. However, a profound insight into the microscopic coupling mechanisms between higher excitonic states and specific excitation pathways can be better gained using nonlinear, multidimensional coherent spectroscopy techniques [23–29]. The method applied in this paper, two-dimensional (2D) double quantum coherence [30–32], offers a direct access to the single-exciton and two-exciton resonances and thus reveals the corresponding excitation pathways and quantum state correlations. *We show that the spectroscopic features visible in 2D spectra reveal the Förster and Dexter coupling characteristics and the limitations imposed on the optical selection rules in the nonlinear response.*

This paper is organized as follows: First, the basic Hamiltonian is discussed. The coupling elements between the quantum dot nanostructures are determined by using the effective mass and envelope function approximation and performing a dipole approximation on the unit cells. After that, the delocalized exciton basis is presented and the linear and nonlinear optical signals are introduced. We finally discuss the characteristic features of our calculated spectra. All calculations are based on the Liouville diagrams [30,32], which serve as an elegant theoretical formulation of the problem.

II. MODEL SYSTEM

The system considered in our work contains two nanostructures labeled 1 and 2 that are coupled via Coulomb interaction. As an example, Fig. 1(a) shows a coupled quantum dot system. In the following, we will focus on the energetically lowest light-induced transitions between the highest occupied and the lowest unoccupied electronic states of each structure such

*marten.richter@tu-berlin.de

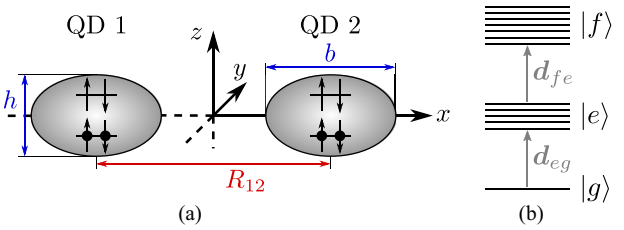

FIG. 1. (Color online) (a) Two coupled QDs as spin-degenerate two-level systems. (b) Three-band model containing the ground state ($|g\rangle$) and single-exciton ($|e\rangle$) and two-exciton states ($|f\rangle$).

that both quantum emitters can be described as two-level systems. In the case of a quantum dot (QD), the energetically lowest allowed electronic transition occurs between its highest occupied valence (v) and lowest unoccupied conduction (c) band state. This transition constitutes the lowest bound exciton.

The single particle electronic wave functions of a double quantum dot system are described using the effective mass and envelope function approximation [33,34]. Here, the wave functions are written as products of the lattice periodic Bloch function $u_{\lambda n\sigma,\boldsymbol{k}\approx 0}(\boldsymbol{r})$ and the envelope function $\xi_{\lambda n}(\boldsymbol{r})$ of an electron with spin $\sigma \in \{\uparrow,\downarrow\}$ in the valence or conduction band $\lambda \in \{v,c\}$ of nanostructure $n \in \{1,2\}$: $\psi(\boldsymbol{r}) = \sum_{\lambda,n,\sigma} \xi_{\lambda n}(\boldsymbol{r}) u_{\lambda n\sigma}(\boldsymbol{r}) a_{\lambda n\sigma}$. $\xi_{\lambda n}(\boldsymbol{r})$ solves the single-particle Schrödinger equation for the confinement potential $U_C(\boldsymbol{r})$ of the QD structure: $[-\hbar^2\nabla^2/(2m^*) + U_C(\boldsymbol{r})]\xi_{\lambda n}(\boldsymbol{r}) = E_{\lambda n}\xi_{\lambda n}(\boldsymbol{r})$. m^* denotes the valence or conduction band effective mass, respectively. For InAs/GaAs QD systems, they are well described by the GaAs bulk effective masses due to the strong strain and confinement conditions affecting the InAs dots [35,36].

For our analysis, we choose a model system consisting of two self-organized ellipsoidal InAs/GaAs QDs as shown in Fig. 1(a). However, our results are not limited to a specific QD system and similar coupling identifying absorption patterns are expected for other coupled nanostructures such as excitons in inorganic sheets coupled to molecular excitons. $U_C(\boldsymbol{r})$ is separated into the three spatial directions $U_C(\boldsymbol{r}) = U_C(x) + U_C(y) + U_C(z)$. The potentials in the y and z directions are assumed to be harmonic (minima at $y,z = 0$) [37]. The ground-state dynamics of the envelope functions $\xi^y_{\lambda n}(y)$ and $\xi^z_{\lambda n}(z)$ is thus given by Gaussian wave functions of widths b in the y direction and h in the z direction [cf. Fig. 1(a)]. The confinement potential in the x direction exhibits two minima at the QD centers with center-to-center distance R_{12}. Its shape is described by two Gaussian functions [37] for our model system:

$$U_C(x) = -U_0 \exp\left[-\frac{1}{2}\left(\frac{x + R_{12}/2}{l_{0,x}}\right)^2\right] - (U_0 + \Delta U)\exp\left[-\frac{1}{2}\left(\frac{x - R_{12}/2}{l_{0,x}}\right)^2\right] \quad (1)$$

with depth U_0 and width $l_{0,x} = b/(2\sqrt{2\ln 2})$. Due to its continuity, this model potential allows an exchange of electrons between the two nanostructures. The corresponding one-dimensional (1D) Schrödinger equation for $\xi^x_{\lambda n}(x)$ is solved numerically using eighth-order finite differences [38].

TABLE I. Material and quantum dot model parameters.

Medium relative permittivity [39]	ϵ_r	10,9
Conduction band eff. mass	m_e^*	$0{,}07\, m_0$
Heavy-hole valence band eff. mass	m_h^*	$0{,}45\, m_0$
Conduction band confinement depth [40]	U_0^c	770 meV
Conduction band potential offset	ΔU^c	−0.5 meV
Valence band confinement depth [40]	U_0^v	330 meV
Valence band potential offset	ΔU^v	−0.05 meV
QD lateral extension	b	5 nm
QD height	h	2.5 nm

For small interdot separations, the resulting single-particle wave functions are not well localized at a particular QD due to the wave-function tunneling. Nevertheless, the two lowest eigenstates $\xi^x_{\lambda 1}$ and $\xi^x_{\lambda 2}$ represent the single-particle states predominantly localized at the lower-energy QD 1 and the higher-energy QD 2, respectively. Consequently, the index n labels the single-particle states that, strictly speaking, do not entirely reside within a particular QD. The full envelope function is given by the product $\xi_{\lambda n}(\boldsymbol{r}) = \xi^x_{\lambda n}(x)\xi^y_{\lambda n}(y)\xi^z_{\lambda n}(z)$. As both Förster and Dexter coupling strengths are very sensitive to the interdot separation, it is preferable to choose small QDs for an increased coupling strength since the distance between the two QD volumes can be relatively small compared to their size. All material and model system parameters are given in Table I.

III. HAMILTON OPERATOR

The full Hamilton operator consists of three contributions: $H = H_0 + H_C + H_{e\text{-}L}$. The free-electron part H_0 contains the undisturbed electronic eigenenergies $\varepsilon_{\lambda n\sigma}$:

$$H_0 = \sum_{\lambda,n,\sigma} \varepsilon_{\lambda n\sigma} a^\dagger_{\lambda n\sigma} a_{\lambda n\sigma}. \quad (2)$$

$a_{\lambda n\sigma}$ and $a^\dagger_{\lambda n\sigma}$ denote the annihilation and creation operators of an electron with spin σ in level λ of the nth single-particle state. Since the spin-orbit coupling is often weak compared to the homogeneous linewidth (which is typically in the order of few μeV for the zero phonon line [41,42]), the spin-up and -down states of the same band within one QD are considered degenerate in this paper: $\varepsilon_{\lambda n\uparrow} = \varepsilon_{\lambda n\downarrow}$. The Coulomb Hamiltonian H_C is given by

$$H_C = \sum_{\substack{\lambda_a \ldots \lambda_d \\ n_a \ldots n_d \\ \sigma_a \ldots \sigma_d}} V_{abcd}\, a^\dagger_{\lambda_a n_a \sigma_a} a^\dagger_{\lambda_b n_b \sigma_b} a_{\lambda_d n_d \sigma_d} a_{\lambda_c n_c \sigma_c} \quad (3)$$

with the Coulomb-coupling matrix element

$$V_{abcd} = \frac{e^2}{8\pi\epsilon_0\epsilon_r} \int d^3r \int d^3r'\, u^*_{\lambda_a n_a \sigma_a}(\boldsymbol{r}) u^*_{\lambda_b n_b \sigma_b}(\boldsymbol{r}') \times \frac{\xi^*_{\lambda_a n_a}(\boldsymbol{r}) \xi^*_{\lambda_b n_b}(\boldsymbol{r}') \xi_{\lambda_d n_d}(\boldsymbol{r}') \xi_{\lambda_c n_c}(\boldsymbol{r})}{|\boldsymbol{r} - \boldsymbol{r}'|} \times u_{\lambda_d n_d \sigma_d}(\boldsymbol{r}') u_{\lambda_c n_c \sigma_c}(\boldsymbol{r}) \delta_{\sigma_a \sigma_c} \delta_{\sigma_b \sigma_d}, \quad (4)$$

where e is the elementary charge, ϵ_0 the vacuum permittivity, and ϵ_r the medium relative permittivity. The two Kronecker deltas ensure spin conservation for the Coulomb interaction.

The Coulomb coupling contains contributions within each single nanostructure and between the two nanostructures. Here, we focus on the discussion of the coupling between the nanostructures ($n_a \neq n_b$). However, all inner QD couplings are included in an analogous way. A Taylor expansion around the center of each elementary cell of the Green's function $G(\boldsymbol{r},\boldsymbol{r}') = \frac{1}{4\pi\epsilon_0\epsilon_r|\boldsymbol{r}-\boldsymbol{r}'|}$ in Eq. (4) gives three types of matrix elements (cf. Appendix): the zeroth-order contribution leads to the so-called monopole-monopole shifts and Dexter elements, the dipole-dipole terms describe the Förster elements. The corresponding coupling elements are derived in detail in the Appendix.

The diagonal monopole-monopole part of the Coulomb Hamiltonian has the form

$$H_C^{\text{mono}} = \sum_{\substack{\lambda_a,\lambda_b,n_a,\\ n_b,\sigma_a,\sigma_b}} V_{abab}^{\text{mono}}\, a^\dagger_{\lambda_a n_a \sigma_a} a^\dagger_{\lambda_b n_b \sigma_b} a_{\lambda_b n_b \sigma_b} a_{\lambda_a n_a \sigma_a}. \quad (5)$$

It represents the electrostatic Coulomb interaction between two charge densities of the electronic states [cf. Eq. (A4)]. The monopole-monopole shifts induce an energy renormalization with respect to the isolated system due to Coulomb interaction. However, monopole-monopole shifts do not describe excitation transfer [14]. All monopole-monopole shifts are included in the calculations of the electronic Hamilton matrix. (Therefore, also single-exciton and biexciton shifts are included in the monopole-monopole part.) The shifts do not strongly alter the eigenstates and are diagonal in the exciton states constructed from the single-particle states. When speaking of the uncoupled system and interaction shifted system energies throughout this paper, we thereby refer only to the off-diagonal couplings such as Förster and Dexter interaction. The diagonal Coulomb couplings are always included in the "uncoupled basis."

The off-diagonal dipole-dipole part of the Coulomb Hamiltonian has the form ($n_a \neq n_b$)

$$H_C^{\text{Förster}} = \sum_{\sigma_a,\sigma_b} V^F_{\sigma_a\sigma_b}\, a^\dagger_{v1\sigma_a} a^\dagger_{c2\sigma_b} a_{v2\sigma_b} a_{c1\sigma_a} + \text{H.c.} \quad (6)$$

with the matrix elements

$$V^{\text{F}}_{\sigma_a\sigma_b} = \frac{1}{4\pi\epsilon_0\epsilon_r} \int d^3r \int d^3r' \left(\frac{\boldsymbol{d}_{vc}^{1\sigma_a} \cdot \boldsymbol{d}_{cv}^{2\sigma_b}}{|\boldsymbol{r}-\boldsymbol{r}'|^3} - 3\frac{\left[\boldsymbol{d}_{vc}^{1\sigma_a} \cdot (\boldsymbol{r}-\boldsymbol{r}')\right]\left[\boldsymbol{d}_{cv}^{2\sigma_b} \cdot (\boldsymbol{r}-\boldsymbol{r}')\right]}{|\boldsymbol{r}-\boldsymbol{r}'|^5} \right) \times \xi^*_{v1}(\boldsymbol{r})\xi^*_{c2}(\boldsymbol{r}')\xi_{v2}(\boldsymbol{r}')\xi_{c1}(\boldsymbol{r}). \quad (7)$$

These dipole-dipole terms represent Förster excitation transfer between the two nanostructures [20]. For this dipole-dipole mediated interaction mechanism, no electronic wave-function overlap is required. As can be seen in Eq. (7), the value of a Förster matrix element is determined by the orientation and magnitude of the microscopic interband dipole moments $\boldsymbol{d}_{\lambda\mu}^{n\sigma}$ of the elementary cells. As stated in Refs. [13,39], the expression is beyond the simple point-dipole approximation often used for Förster transfer [12,43] since the dipole approximation is carried out on every unit cell. Furthermore, the distance between the nanostructures does not simply determine the coupling strength, but the distance between all unit cells of the nanostructures weighted by the occupation probability does [cf. Eq. (7)]. The dipole moments depend on the orientation of the crystal lattice [cf. Eq. (A3)]. The structure of $V^F_{\sigma_a\sigma_b}$ shows that the spin of an excited electron changes from σ_a (in structure n_a) to σ_b (in structure n_b) during Förster energy transfer. The dependence of the spin-preserving ($\sigma_a = \sigma_b$) and -flipping ($\sigma_a \neq \sigma_b$) exciton transfer mechanisms (described by the spin dependence of $V^F_{\sigma_a\sigma_b}$) on the mutual orientation of the two coupled nanostructures has been discussed in Refs. [17,44,45] for double QD structures: It was shown that the Förster coupling strength strongly depends on the relative orientation of the QDs if they are arranged in a column as shown in Fig. 2(a). Parallel alignment of the two vertically stacked QDs leads to spin-preserving Förster transfer [$\theta = 0$, see Fig. 2(b)], whereas the exciton spin is flipped during Förster transfer in the case of antiparallel alignment ($\theta = \pi$). In contrast, the Förster coupling elements show no orientational dependence if the QDs are grown in a plane with their crystalline c axes parallel to each other, as depicted in Fig. 1(a). Consequently, Förster coupling is not spin selective if the two QDs are arranged in a row, and the donor exciton couples to both exciton states in the acceptor. We will show that this will lead to more bright single-exciton states than in the case of the stacked growth, caused by the Förster induced hybridization process of the single-exciton states.

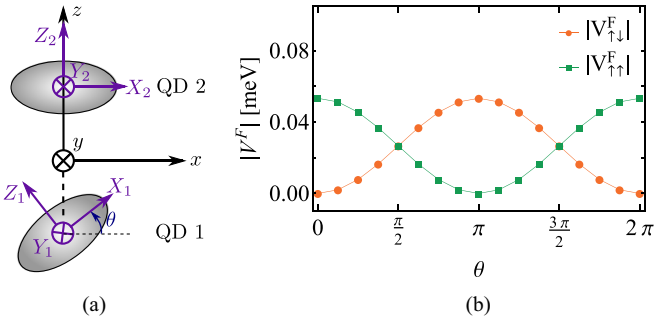

FIG. 2. (Color online) (a) Two QDs aligned in a column with local coordinate systems. θ defines the rotation angle between the QD orientations. (b) Values of a spin-preserving ($|V^F_{\uparrow\uparrow}|$) and a spin-flipping Förster coupling element ($|V^F_{\uparrow\downarrow}|$) as a function of θ.

Rotation angles $\theta \neq 0$ can be realized for systems with tunable relative orientations such as colloidal QDs. In the considered example of two self-assembled QDs grown in a plane or vertical stack, the growth direction is oriented along the host crystal lattice. Therefore, nonparallel dipole moments will only occur as a consequence of light-hole admixture [46], which exceeds the framework of this paper.

In this work, we will include a second type of Coulomb induced excitation energy transfer, the Dexter transfer [16]. As in the case of Förster transfer, Dexter transfer also induces an exciton transfer from the donor to the acceptor, but the underlying mechanism is different: Dexter transfer describes a direct, real exchange of electrons between the structures, which is only possible for overlapping electronic wave functions. Thus, it is only important if the nanostructures are close to each other. The corresponding Dexter part of the Coulomb Hamiltonian is also derived in the Appendix and has the

form

$$H_C^{\text{Dexter}} = \sum_{\sigma_a,\sigma_b} V^{\text{D}}\, a^\dagger_{v1\sigma_a} a^\dagger_{c2\sigma_b} a_{c1\sigma_b} a_{v2\sigma_a} + \text{H.c.} \tag{8}$$

with the coupling elements

$$V^{\text{D}} = \frac{e^2}{4\pi\epsilon_0\epsilon_{\text{r}}} \int d^3r \int d^3r' \, \frac{\xi^*_{v1}(\boldsymbol{r})\xi^*_{c2}(\boldsymbol{r}')\xi_{c1}(\boldsymbol{r}')\xi_{v2}(\boldsymbol{r})}{|\boldsymbol{r}-\boldsymbol{r}'|}. \tag{9}$$

σ_a denotes the spin of the electron transferred from one valence band to the other, while σ_b denotes the spin of the transferred conduction band electron. Because of $\xi^*_{v1}(\boldsymbol{r})\xi_{v2}(\boldsymbol{r})$ and $\xi^*_{c2}(\boldsymbol{r}')\xi_{c1}(\boldsymbol{r}')$, Dexter transfer relies on sufficient wave-function overlap. V^{D} is spin independent and, therefore, each electron keeps its spin state during the transfer: There are only spin-preserving Dexter processes, which is different to the Förster transfer.

Finally, the electron-light interaction $H_{e\text{-}L}$ is treated semiclassically as [33]

$$H_{e\text{-}L} = -\boldsymbol{d}\cdot\boldsymbol{E}(t) \tag{10}$$

with the dipole operator

$$\boldsymbol{d} = \sum_{n,\sigma} \left(\int d^3r\, \xi^*_{vn}(\boldsymbol{r})\xi_{cn}(\boldsymbol{r})\, \boldsymbol{d}^{n\sigma}_{vc}\, a^\dagger_{vn\sigma} a_{cn\sigma} + \text{H.c.} \right). \tag{11}$$

In principle, also spatially indirect excitons originating from light-induced electronic dipole transitions from one QD to the other must be taken into account since we consider a nonvanishing electronic wave-function overlap between the QDs. However, direct excitons with the electron and hole within the same QD are strongly preferred energetically due to Coulomb attraction. Therefore, indirect excitons are not part of the discussion since their excitation energies are several tens of meV above the energy window studied in the spectra and the transitions have only weak oscillator strengths. Nevertheless, these exciton states have been included in all calculations.

For circular polarization of the external field, $\boldsymbol{E}(t)$ can be expressed as $\boldsymbol{E}(t) = E(t)\boldsymbol{e}_{\sigma_\pm}$ with the polarization vectors $\boldsymbol{e}_{\sigma_+}$ and $\boldsymbol{e}_{\sigma_-}$ for right- and left-circularly polarized light. They are given by $\boldsymbol{e}_{\sigma_+} = (\hat{\boldsymbol{e}}_x - i\hat{\boldsymbol{e}}_y)/\sqrt{2}$ and $\boldsymbol{e}_{\sigma_-} = (\hat{\boldsymbol{e}}_x + i\hat{\boldsymbol{e}}_y)/\sqrt{2}$, respectively, where $\hat{\boldsymbol{e}}_x$ and $\hat{\boldsymbol{e}}_y$ are unit vectors in a plane perpendicular to the propagation direction [47].

In order to study the impact of the Coulomb interaction on the eigenenergies of the system and to discuss linear and nonlinear optical properties, we rewrite the Hamiltonian in diagonalized exciton states. The system is assumed to be initially in the ground state $|g\rangle$. The absorption of one photon generates a single-exciton state. The uncoupled, local single-exciton states $|X_i\rangle$ of the individual QDs (n_i) are eigenstates of H_0 and created from the ground state: $|X_i\rangle = a^\dagger_{cn_i\sigma_i} a_{vn_i\sigma'_i}|g\rangle$. In this local basis, the exciton Hamilton operator has only off-diagonal elements for Förster and Dexter coupling elements. Due to these nondiagonal transition matrix elements, the local single-exciton states are hybridized [12,13,48]. By diagonalizing the exciton Hamilton operator, the new delocalized single-exciton basis set $\{|e\rangle\}$ of eigenstates $|e\rangle = \sum_i \eta^e_i |X_i\rangle$ of the electronic Hamiltonian $(H_0 + H_C)|e\rangle = E_e|e\rangle$ and the expansion coefficients η^e_i are obtained.

If two or more photons are absorbed by the system, also double excitons can be excited. In analogy to the single-exciton states, the two-exciton states $|B_{ij}\rangle$ of the uncoupled system are set as $|B_{ij}\rangle = a^\dagger_{cn_i\sigma_i} a_{vn_i\sigma'_i} a^\dagger_{cn_j\sigma_j} a_{vn_j\sigma'_j}|g\rangle$ with $i < j$. The delocalized double-exciton eigenstates are $|f\rangle = \sum_{i,j} \eta^f_{ij}|B_{ij}\rangle$ with energy E_f: $(H_0 + H_C)|f\rangle = E_f|f\rangle$.

Subsequently, we will refer to the delocalized eigenstates of our system as manifolds g (ground state), e (single-exciton states), and f (two-exciton states) [cf. Fig. 1(b)]. Higher-order exciton states excited in wave mixing higher than third order can be formulated in a similar way, but will not be considered in this work since these states do not contribute to the double quantum coherence signal realized in 2D spectroscopy [32] in the $\chi^{(3)}$ limit used to differentiate between Förster and Dexter coupling.

IV. LINEAR OPTICAL SPECTROSCOPY

The linear absorption coefficient at an incident frequency ω is given by [33]

$$\alpha(\omega) = \frac{\omega}{n(\omega)\epsilon_0 c}\, \text{Im}\left(\frac{P^{(1)}(\omega)}{E(\omega)}\right). \tag{12}$$

$n(\omega)$ is the frequency-dependent refractive index of the material {with $n(\omega) \gg \text{Re}[P^{(1)}(\omega)/(\epsilon_0 E(\omega))]$}, c is the speed of light in vacuum. The polarization in first order of the electric field is given by $\boldsymbol{P}^{(1)}(t) = \text{tr}[\boldsymbol{d}\,\rho^{(1)}(t)]$. $\boldsymbol{P}^{(1)}(\omega)$ can be calculated by using the dipole operator $\boldsymbol{d}$ and the first-order density operator $\rho^{(1)}(t)$ in the new delocalized exciton basis. Introducing a phenomenological dephasing constant γ accounting for radiation processes and a Fourier transform of $\boldsymbol{P}^{(1)}(t)$, the linear absorption reads as [32,33]

$$\alpha(\omega) \propto \omega \sum_e |\boldsymbol{d}_{eg}\cdot\boldsymbol{e}_{\text{Pol}}|^2 \, \frac{\gamma}{\gamma^2 + (\omega_{eg}-\omega)^2}. \tag{13}$$

Here, $\boldsymbol{e}_{\text{Pol}}$ denotes the polarization direction of the incoming light, and $\boldsymbol{d}_{eg}$ is the dipole moment between the ground state and a single-exciton state. The matrix element has the form

$$\boldsymbol{d}_{eg} = \langle e|\boldsymbol{d}|g\rangle = \sum_i \eta^{e*}_i \langle X_i|\boldsymbol{d}|g\rangle. \tag{14}$$

$\omega_{eg} \equiv \frac{1}{\hbar}(E_e - E_0)$ denotes the resonance frequencies of the single-excitonic system with ground-state energy E_0. The phenomenological damping is assumed to be $\gamma = 1/(500\,\text{ps})$ [49].

V. MULTIDIMENSIONAL SPECTROSCOPY

In this section, we will investigate heterodyne-detected two-dimensional (2D) signals obtained by a multiple-pulse technique [32]. While in linear spectroscopy only a single excitation of the quantum system is observed, coherent multidimensional spectroscopy allows us to excite double-exciton and higher states and thus study their energies and couplings. We consider coherent spectroscopy with three pulses up to the third order in field.

In the considered four-wave mixing experiment, the system is excited by a sequence of three temporally separated pulses centered at times τ_1, τ_2, and τ_3 with delay times T_1 and T_2 between them (cf. Fig. 3). A spatial separation of the pulses by selecting the directions of the incoming signals (phase matching) can only be realized for spatially extended systems of identical structures and not for a single nanosystem. In the

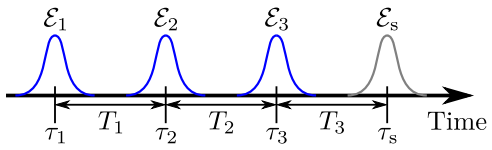

FIG. 3. (Color online) Timeline for the pulse sequence applied in a double quantum coherence experiment.

case of a single nanosystem, the excitation pathways can be controlled using phase cycling, where the phase shifts between the pulses are varied [24]. The optical field then reads as [32]

$$\boldsymbol{E}(\boldsymbol{r},t)=\sum_{j=1}^{3}\sum_{u_j=\pm1}\mathcal{E}_j^{u_j}(\boldsymbol{r},t-\tau_j)e^{-iu_j\omega_j(t-\tau_j)+iu_j\varphi_j} \tag{15}$$

with the envelope $\mathcal{E}_j^{u_j}(t-\tau_j)$ of the jth pulse with phase φ_j and laser frequency ω_j. The u_j can either take the value $+1$ or -1 with $\mathcal{E}_j^{-1}=(\mathcal{E}_j^{+1})^*$. The phase of a specific signal is given by a particular linear combination of the incident pulse phases φ_j: $\varphi_s=u_1\varphi_1+u_2\varphi_2+u_3\varphi_3$. The factors $u_j=\pm1$ are chosen according to the extracted phase combination, in our case for the DQC signal. Other possible signals such as the photon echo are described in Ref. [23].

Here, it is sufficient to consider the three lowest manifolds g, e, and f. In this case, the polarization in third order of the electric field is the observable [32]

$$\begin{aligned}P_\alpha^{(3)}(\boldsymbol{r},t)&\\ =\int_0^\infty\int_0^\infty\int_0^\infty dt_3dt_2dt_1&\sum_{\beta,\gamma,\delta=1}^{3}R^{(3)}_{\alpha\beta\gamma\delta}(t_3,t_2,t_1)\\ \times E_\beta(\boldsymbol{r},t-t_3)E_\gamma(\boldsymbol{r},t-t_3-t_2)&E_\delta(\boldsymbol{r},t-t_3-t_2-t_1).\end{aligned} \tag{16}$$

$R^{(3)}_{\alpha\beta\gamma\delta}(t_3,t_2,t_1)$ is the third-order response function (see Refs. [30,32]) and t_1, t_2, and t_3 denote the time intervals between the interactions with the optical fields.

We will focus on double quantum coherence (DQC) signals $S_{\varphi_{\rm III}}$ with a signal phase $\varphi_{\rm III}=\varphi_1+\varphi_2-\varphi_3$ and frequency $\omega_s=\omega_1+\omega_2-\omega_3$. The two possible Liouville space pathways contributing to the response function and thus to the DQC signal are illustrated in Fig. 4 using double-sided Feynman diagrams [30]. It can be seen on the diagrams that the first two

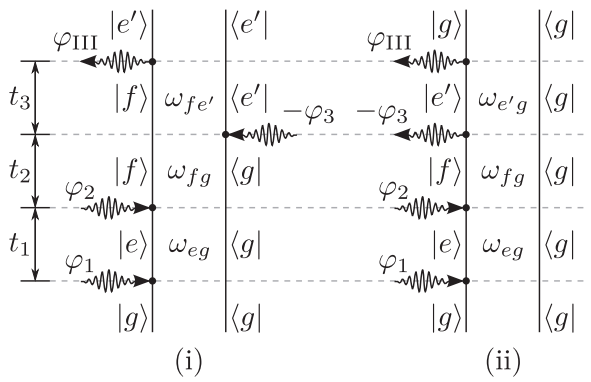

FIG. 4. Feynman diagrams showing the two Liouville pathways (i) and (ii) of the density matrix for the DQC signal $\varphi_{\rm III}$.

interactions induce the same changes in the density matrix in both pathways: During the time interval t_1, the density matrix is in a coherence between the ground state g and a single exciton state e, oscillating at an optical frequency ω_{eg}. The second pulse generates a coherence between the ground state and a two-exciton state f. Only after the third laser pulse φ_3, the two pathways differ: It creates a $|f\rangle\langle e'|$ coherence in pathway (i) and a $|e'\rangle\langle g|$ coherence in pathway (ii). The last, outgoing pulse $\varphi_{\rm III}$ represents the so-called local oscillator field which is mixed with the signal field for heterodyne detection [32].

The third-order signal depends on the three delay times T_1, T_2, and T_3 between the pulses (Fig. 3) and has the form [32]

$$S^{(3)}_{\varphi_{\rm III}}(T_3,T_2,T_1)=\int_{-\infty}^{+\infty}dt\;\boldsymbol{P}_{\varphi_{\rm III}}(t)\cdot\mathcal{E}_s^*(t-\tau_s)e^{i\omega_s(t-\tau_s)}. \tag{17}$$

Here, $\mathcal{E}_{\rm s}$ denotes the local oscillator field and $\boldsymbol{P}_{\varphi_{\rm III}}(t)$ is the induced polarization of the DQC signal. It depends on the corresponding response function representing the Liouville pathway contributing to the $\varphi_{\rm III}$ technique (Fig. 4). The DQC 2D signal is measured as a function of the excitation frequencies Ω_1 and Ω_2, which is obtained by Fourier transforming the signal $S_{\varphi_{\rm III}}(T_3,T_2,T_1)$ with respect to the pulse delays T_1 and T_2 at a fixed third time interval T_3. The double quantum coherence signal is composed of the two contributions from pathways (i) and (ii):

$$S^{(3)}_{\varphi_{\rm III}}(T_3,\Omega_2,\Omega_1)=S^{(3)}_{i}(T_3,\Omega_2,\Omega_1)+S^{(3)}_{ii}(T_3,\Omega_2,\Omega_1) \tag{18}$$

with the contributions [32]

$$\begin{aligned}S^{(3)}_{i}(T_3,\Omega_2,\Omega_1)=-i\frac{(2\pi)^4}{\hbar^3}&\sum_{e,e',f}[\boldsymbol{d}^*_{fe'}\cdot\mathcal{E}^*_{\rm s}(\omega_{fe'}-\omega_s)]\\ &\times[\boldsymbol{d}^*_{e'g}\cdot\mathcal{E}^*_3(\omega_{e'g}-\omega_3)e^{-i\xi_{fe'}T_3}]\\ &\times\frac{\boldsymbol{d}_{fe}\cdot\mathcal{E}_2(\omega_{fe}-\omega_2)}{\Omega_2-\xi_{fg}}\frac{\boldsymbol{d}_{eg}\cdot\mathcal{E}_1(\omega_{eg}-\omega_1)}{\Omega_1-\xi_{eg}},\end{aligned} \tag{19}$$

$$\begin{aligned}S^{(3)}_{ii}(T_3,\Omega_2,\Omega_1)=i\frac{(2\pi)^4}{\hbar^3}&\sum_{e,e',f}[\boldsymbol{d}^*_{e'g}\cdot\mathcal{E}^*_{\rm s}(\omega_{e'g}-\omega_s)]\\ &\times[\boldsymbol{d}^*_{fe'}\cdot\mathcal{E}^*_3(\omega_{fe'}-\omega_3)e^{-i\xi_{e'g}T_3}]\\ &\times\frac{\boldsymbol{d}_{fe}\cdot\mathcal{E}_2(\omega_{fe}-\omega_2)}{\Omega_2-\xi_{fg}}\frac{\boldsymbol{d}_{eg}\cdot\mathcal{E}_1(\omega_{eg}-\omega_1)}{\Omega_1-\xi_{eg}}.\end{aligned} \tag{20}$$

In analogy to the linear case, $\boldsymbol{d}_{eg}$ and $\boldsymbol{d}_{fe}$ represent the ground state to single exciton and single exciton to biexciton transition dipole moments in the delocalized exciton basis, respectively: $\boldsymbol{d}_{fe}=\sum_{i,j}\eta_{ij}^{f\,*}\langle B_{ij}|\hat{\boldsymbol{d}}|X_j\rangle\eta_j^e$. The $\xi_{ab}\equiv\omega_{ab}-i\gamma_{ab}$ take into account the dephasing rate γ_{ab} and the exciton frequencies $\omega_{eg}=\frac{1}{\hbar}(E_e-E_0)$ and $\omega_{fe}=\frac{1}{\hbar}(E_f-E_e)$.

The resonances that occur in the 2D spectra [Eqs. (19) and (20) as functions of Ω_1 and Ω_2] reveal how the single-exciton (ω_{eg}) and two-exciton states (ω_{fe}) of the investigated system are connected: Their intensities indicate the contribution of a single-exciton resonance (Ω_1 axis) to a specific two-exciton

state (Ω_2 axis) [31]. The resonances projected on the single-exciton Ω_1 axis (for $\Omega_2 = \omega_{fe}$) coincide with the signals obtained by linear absorption spectroscopy. The signatures along the Ω_2 axis provide additional information about the two-exciton resonances after excitation with a second laser pulse at frequency Ω_2: In coupled, hybridized quantum systems, they reveal specific single-exciton to two-exciton excitation pathways that could not be accessed in uncoupled systems due to the optical selection rules.

VI. DISCUSSION OF THE OPTICAL SPECTRA

We now discuss the linear and two-dimensional DQC optical spectra [Eqs. (18)–(20) as a function of Ω_1 and Ω_2]. The single- and two-exciton energy scales are given as detuning with respect to the uncoupled resonance energies for the creation of a single exciton (E_1) and biexciton (E_{11}) at the QD with lower band-gap energy (referred to as QD 1), respectively. The detuning Δ between the original resonance energies of the two QDs follows from the potential offsets $\Delta U^{c/v}$ after diagonalization. In order to observe both weak and strong signatures on the same scale, the following nonlinear scaling was chosen [50]: $\mathcal{S}_{\text{nonlinear}} = \text{arsinh}(|S^{(3)}_{\varphi_{\text{III}}}|/N)$ with normalization constant N.

In the example, the optical excitation pathways follow the zinc-blende selection rules. Only exciton states with opposite spins of electron and hole have a finite dipole transition moment and can thus be directly excited by optical pulses. These excitons are called bright single excitons. In the local exciton basis, four bright single-exciton configurations exist, two in each QD (states X_1 to X_4 in Fig. 5). Furthermore, it is possible to selectively excite a specific conduction band spin state by the use of circularly polarized light [51,52].

In order to interpret the optical spectra, it is essential to know the two-exciton configurations which can be excited directly from the bright single excitons with different circularly polarized optical pulses. The possible excitation pathways are shown in Fig. 6. If the system absorbs two photons of the same circular polarization, only one two-exciton state composed of two single excitons with the same electron spin at different QDs can be created. In Figs. 5 and 6, this two-exciton state is denoted as B_5 in the case of right-hand

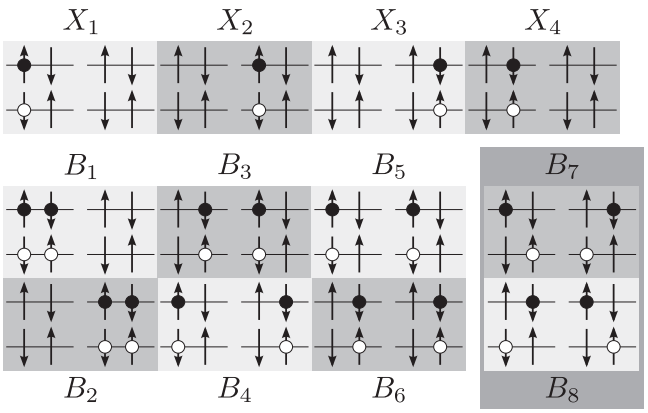

FIG. 5. Configurations of the four bright single excitons X_1 to X_4, the six bright two-excitons B_1 to B_6 and of two dark double excitonic states B_7 and B_8 (right, darkened column).

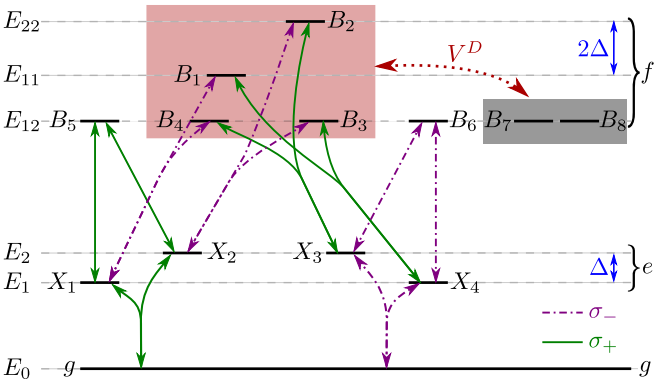

FIG. 6. (Color online) Level scheme showing the possible excitation pathways in the uncoupled system. E_0 denotes the energy of the ground state g, E_n the energy of the uncoupled single-exciton states X_i at QD n, and E_{mn} the energy of the local double-exciton states B_i consisting of two excitons at QDs m and n (m,n = 1,2). The energetic distance between the uncoupled single-exciton energies E_1 and E_2 corresponds to the band-gap detuning Δ between the QDs, the uncoupled biexciton energies E_{11} and E_{22} are separated by 2Δ. The purple and green arrows indicate the possible transitions for excitation with left-hand and right-hand circularly polarized light, respectively. The dotted red arrow labeled V^{D} marks the Dexter coupling of the four bright two-exciton states B_1 to B_4 (red box) to the dark two-exciton states B_7 and B_8.

circular polarization and as B_6 in the case of left-hand circular polarization. An excitation with two laser pulses of opposite circular polarizations can generate so-called biexciton states with both electron-hole pairs at the same QD (B_1 and B_2) as well as configurations with both excitons at different QDs (B_3 and B_4). Since spin-orbit coupling is neglected, B_3 and B_4 are energetically degenerate. Regarding the uncoupled system, three two-exciton resonance energies are expected: In the spectra shown later, the double-exciton resonances are denoted E_{11} (for the state B_1), E_{22} (for B_2), and E_{12} (for the states B_3 to B_6 with the two excitons at different QDs), as shown in Fig. 6.

Of course, the nondiagonal Coulomb couplings relax these strict optical selection rules discussed above due to hybridization in the formation process of delocalized states. The diagonalized eigenenergies of the system are denoted e_i for single excitons and f_i for two excitons. The energies of the coupled system are shifted with respect to the resonance energies of the uncoupled system which are marked by dashed lines in the spectra (next section). In some cases, some excitons are not hybridized and thus their energy remains unchanged.

For the discussion, we distinguish the following cases:

A. Case 1: Dominantly Förster coupled system

In this case, the QDs are separated in a way that the QDs have negligible Dexter transfer compared to the Förster elements. Here, a higher value $d = 1.3\,\text{e nm}$ of the dipole moment compared to case 2 was set for the numerical calculation in order to discuss the thus increased Förster coupling in more detail. This value is slightly higher than the values between 0.3 and 0.9 e nm usually found in literature [39,53–55] (dipole moments of magnitudes 1 to 2 e nm have

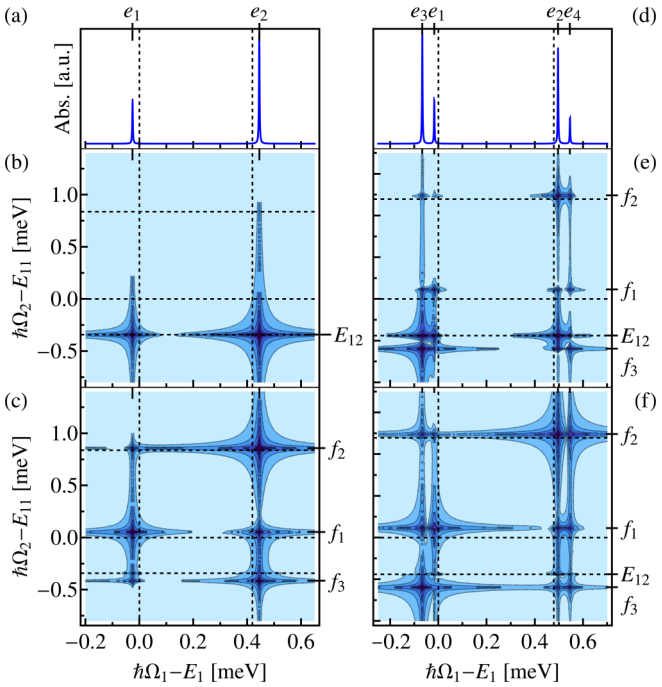

FIG. 7. (Color online) Case 1(i) (left column, only spin-preserving Förster coupling) and 1(ii) (right column, spin-preserving and -flipping Förster coupling): Linear absorption spectra [(a) and (d)] and 2D spectra for excitation with four laser pulses of identical circular polarizations $\sigma_+\sigma_+\sigma_+\sigma_+$ [(b) and (e)] and alternating polarizations $\sigma_+\sigma_-\sigma_+\sigma_-$ [(c) and (f)]. All DQC signals were calculated for a fixed delay time $T_3 = 1$ ps.

so far only been measured for single QDs, cf. Ref. [56]). We further distinguish the following:

(i) The QDs at center-to-center distance $R_{12} = 12$ nm are aligned in a stack with parallel orientation [cf. Fig. 2(a)]. In this geometry, spin is conserved during Förster transfer. The corresponding coupling element is calculated as $|V^{\mathrm{F}}_{\uparrow\uparrow}| = |V^{\mathrm{F}}_{\downarrow\downarrow}| = 0.11$ meV.

(ii) The QDs are arranged in a plane [cf. Fig. 1(a)] with $R_{12} = 13$ nm, where both spin-preserving and spin-flipping Förster transfers occur with the respective calculated coupling elements $|V^{\mathrm{F}}_{\uparrow\uparrow}| = |V^{\mathrm{F}}_{\downarrow\downarrow}| = 0.050$ meV and $|V^{\mathrm{F}}_{\uparrow\downarrow}| = |V^{\mathrm{F}}_{\downarrow\uparrow}| = 0.14$ meV.

For case 1(i), where spin-preserving Förster interaction is the only coupling, one bright single exciton is always coupled to the bright single exciton with corresponding spin state in the other QD [cf. Fig. 9(a)]. This leads to a hybridization of the two bright excitons and thus two interaction shifted peaks in the linear absorption spectrum of Fig. 7(a). The upper resonance exhibits a higher oscillator strength than the lower peak [13].

Figures 7(b) and 7(c) show the 2D spectra for two different polarization combinations of the four exciting pulses: $\sigma_+\sigma_+\sigma_+\sigma_+$ and $\sigma_+\sigma_-\sigma_+\sigma_-$. As pointed out before, exciting the system with photons of the same, right-hand circular polarization [Fig. 7(b)] leads to one bright two-exciton state B_5 with both spin-up excitons at different QDs. The corresponding excitation pathways shown in Fig. 6 consist of two sequent green arrows lifting the system from the ground state to B_5. This double-exciton state cannot couple to any other two-exciton states by means of $V^{\mathrm{F}}_{\uparrow\uparrow}$ since all spin-up electrons are already excited. Hence, Fig. 7(b) shows only one two-exciton resonance, which is not changed by Förster coupling with respect to the uncoupled resonance E_{12}. In contrast, an excitation with four pulses of alternating polarizations, e.g., $\sigma_+\sigma_-\sigma_+\sigma_-$ [Fig. 7(c)], leads to three dominant two-exciton resonances. They result from the excitation of two electron-hole pairs within the same QD (state B_1 at energy f_1 for QD 1, state B_2 at energy f_2 for QD 2) and the excitation of one electron-hole pair in each QD (states B_3 and B_4 at energy f_3). All three states are coupled via spin-preserving Förster transfer and therefore change their energy with respect to the uncoupled resonances E_{11}, E_{22}, and E_{12} (dashed lines) due to Förster coupling (cf. Fig. 6). It is noteworthy that in particular the peaks at e_2/f_1 and e_1/f_2 mark excitation pathways that could not be excited if there were no Förster coupling since the electron-hole pair generated by the first pulse has to be transferred to the other QD via Förster coupling.

In case 1(ii) [Figs. 7(d)–7(f)], both spin-preserving and spin-flipping Förster transfers occur. Thus, in linear spectroscopy one bright single exciton in one of the QDs couples to both bright single excitons in the other QD and a hybridization of all four bright single excitons can be observed in Fig. 7(d) (upper panel). In the nonlinear regime, also the two-exciton states are important. All six bright two-exciton configurations are coupled via Förster transfer. If the system is excited by photons of the same polarization, a weak coupling from B_5 (see Fig. 6) to the biexciton states B_1 (energy f_1) and B_2 (energy f_2) is observed in Fig. 7(e) due to spin-flipping Förster coupling. The third, low-energy resonance splits into two closely spaced two-exciton resonances at the hybridized level f_3 and the uncoupled resonance E_{12}, where the E_{12} line exhibits only a weak oscillator strength for $\sigma_+\sigma_-\sigma_+\sigma_-$ excitation. The symmetry of the bright two-exciton configurations with electron-hole pairs at different QDs (B_3 to B_6) causes, that the Förster shifts are canceled, which results in an additional absorption peak at the uncoupled resonance E_{12}. The spectrum for excitation with alternating polarizations [Fig. 7(f)] shows a 4×4 peak pattern as well due to the coupling of all bright two-exciton configurations. In comparison to Fig. 7(e), the two-exciton resonances at f_1 and f_2 exhibit higher intensities since the contributing dipole moments are increased.

In principle, a cancellation of the Förster shifts for some delocalized states and thus an additional peak at the uncoupled resonance E_{12} might also occur in case 1(i) for $\sigma_+\sigma_-\sigma_+\sigma_-$ excitation due to the symmetry of the two-exciton states B_3 and B_4. However, the corresponding two-exciton resonance has only a low oscillator strength and is therefore hardly visible in the spectrum.

B. Case 2: Predominantly Dexter coupled system

In this case, the QDs are arranged in a plane in close proximity ($R_{12} = 10$ nm) with negligible Förster coupling (calculated as $|V^{\mathrm{F}}| \approx 0.02$ meV) compared to the calculated dominant Dexter interaction strength $V^{\mathrm{D}} = 1.6$ meV. The QD dipole moment is chosen to be $d = 0.6$ e nm [54]. Since Dexter interaction always preserves the spin state of the transferred exciton, a bright single exciton in one QD couples to the bright exciton with the same spin state in the other QD. This results in the same linear absorption features as in case 1(a), but this

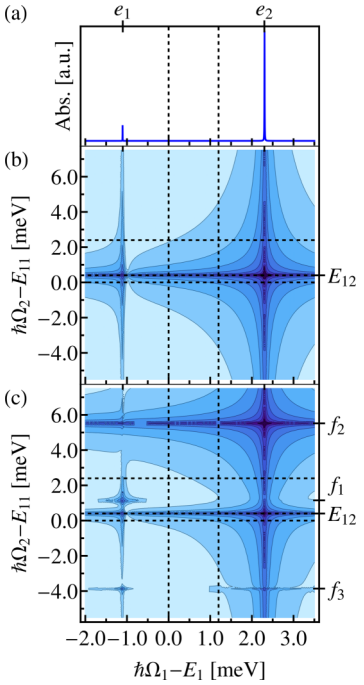

FIG. 8. (Color online) Case 2 (dominant Dexter coupling): Linear absorption spectrum (a) and 2D spectra for excitation with four laser pulses of identical circular polarizations $\sigma_+\sigma_+\sigma_+\sigma_+$ (b) and alternating polarizations $\sigma_+\sigma_-\sigma_+\sigma_-$ (c). Due to the Dexter coupling, the peaks are strongly shifted with respect to the uncoupled resonances (dashed lines) and the lower resonance single-exciton peak at -1.1 meV nearly vanishes (*dark state*). Therefore, the same nonlinear scaling as for the 2D spectra was chosen for the linear spectrum. All DQC signals were calculated for a fixed delay time $T_3 = 1$ ps.

time the energy shift induced by the coupling is determined by the Dexter interaction strength [cf. Fig. 8(a)].

The 2D spectrum for excitation with identical polarizations $\sigma_+\sigma_+\sigma_+\sigma_+$ [Fig. 8(b)] exhibits the same features as the corresponding spectrum in case 1(i), where spin-preserving Förster processes constitute the only coupling mechanism. In analogy to the Förster case 1(i), only one two-exciton absorption resonance is observed at the uncoupled resonance E_{12} since no Dexter excitation transfer is possible when both spin-up conduction band states of the two QDs are occupied. Here, the spin-preserving Förster and Dexter coupling mechanisms open the same excitation transfer channels in the system.

This changes in the case of an excitation with alternating photon polarizations $\sigma_+\sigma_-\sigma_+\sigma_-$ in Fig. 8(c): Here, a splitting of the low-energy resonance into two peaks at f_3 and E_{12} can be observed, where the interaction shifted resonance at f_3 has only a low oscillator strength compared to the uncoupled E_{12} resonance. Therefore, the oscillator strength distribution between these two peaks is inverted compared to the purely Förster coupled case in Fig. 7(c), where the uncoupled resonance E_{12} is vanishing or has minor oscillator strength. This effect is specific to Dexter coupling: *Besides the coupling between bright single excitons of the same spin state like spin-preserving Förster interaction, Dexter transfer can also cause a coupling between bright and dark two-exciton states.* Figure 9(b) shows a schematic representation of Dexter

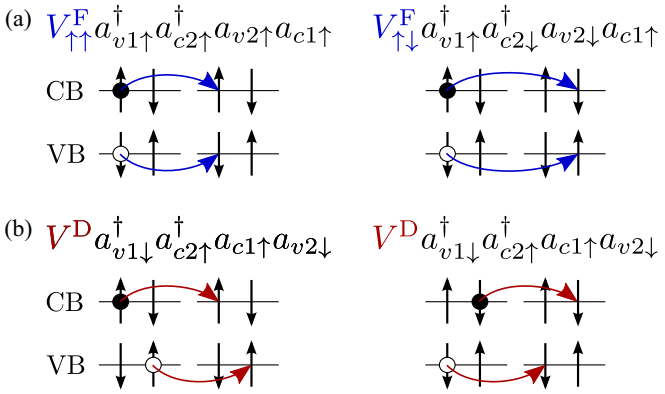

FIG. 9. (Color online) (a) Spin-preserving and -flipping Förster coupling schemes. (b) Dexter coupling between dark exciton states.

coupling mechanisms between dark electron-hole pairs. If a biexciton localized at one of the QDs is excited, this state can be Dexter coupled to a two-exciton state with a dark electron-hole pair in each QD. This leads to a Dexter coupling between four bright (B_1 to B_4) and two dark (B_7 and B_8) two-exciton states, as can be seen in Fig. 6. Again, the corresponding Dexter shifts are canceling for multiple couplings between these states for some delocalized states, which leads to an additional hybridized two-exciton state occurring at the uncoupled resonance E_{12}. This peak exhibits a high oscillator strength compared to the interaction shifted peak at f_3 since Dexter transfer to dark two-exciton states changes the overall structure of formed exciton eigenstates. Specifically for some states, their internal distribution over dark and bright two-exciton states leads to a cancellation of the interaction shifts due to multiple couplings. This results in an enhanced oscillator strength of the resonance E_{12} for predominantly Dexter coupled systems.

If an intermediate distance between the QDs is chosen such that both Förster and Dexter couplings are important, we essentially observe the same behavior as in case 1(ii) without Dexter processes, only that the spin-preserving Förster transfer mechanisms are enhanced by the additional Dexter interactions. This leads to a stronger splitting of the absorption peaks, whereas the number of resonances is the same.

In summary, we observed the following 2D absorption peak patterns, which identify the nature of coupling processes: In case 1(i) (only spin-preserving Förster coupling), we obtained a 1×2 pattern for $\sigma_+\sigma_+\sigma_+\sigma_+$ excitation due to the coupling of the two bright single excitons with identical spin states and no two-exciton coupling. For $\sigma_+\sigma_-\sigma_+\sigma_-$ excitation, three interaction shifted two-exciton resonances are observed because of the additional coupling to the biexcitonic states. In case 1(ii) (spin-preserving and -flipping Förster coupling), a 4×4 pattern for both polarization combinations emerged as a consequence of the coupling of all bright single excitons and the splitting of the low-energy two-exciton resonance due to the hybridization of all bright two excitons. Case 2 (dominant Dexter coupling) revealed a 1×2 pattern for $\sigma_+\sigma_+\sigma_+\sigma_+$ excitation [same behavior as in case 1(a)] and a 4×2 pattern with substantially increased peak intensity at E_{12} for $\sigma_+\sigma_-\sigma_+\sigma_-$ excitation because of Dexter coupling to dark two-exciton states. These spectroscopic signatures are unique

and help to distinguish the different coupling mechanisms by using 2D spectroscopy.

Overall, the different Coulomb coupling mechanisms, in particular in Figs. 7(c) and 8(c), exhibit their characteristic features in fine details of the 2D resonance peak structure (like the intensity distribution between the two low-energy resonances at energies f_3 and E_{12}). Therefore, a careful analysis of the resonance patterns and peak intensities and a sufficient experimental resolution are crucial for a reliable identification of the underlying coupling processes. Modern, ultrafast laser systems (see, e.g., Refs. [57–59]) allow for a femtosecond pulse delay control, which is short compared to dephasing processes. However, shifts due to spectral diffusion will in principle affect spectroscopic measurements of single nanostructures since high repetition rates and thus long integration times are required for a sufficient resolution [49,60]. This sampling problem can be addressed, e.g., by applying suitable apodization schemes [61]. In the last few years, four-wave mixing experiments with homogeneous linewidths between 20 and 50 μeV have been performed [49,62,63], such that Coulomb couplings in the order of 1 meV (like the Dexter coupling strength calculated for our model system) should in principle be visible for slightly detuned single QD systems in modern 2D experiments. Aside from experimental studies on an ensemble of QDs [63], also studies using coherent spectroscopy on single natural QDs in a quantum well were carried out [62] for a photon echo. In principle, similar coherences as in the double quantum coherence spectrum can be detected in photon echo spectra, but DQC dissects the resonances better. Overall, it shows that studies of coherent spectroscopy on single systems are possible.

Another point may be important if light-hole admixture is taken into account (see, e.g., Refs. [51,64]). Then, additional excitation pathways are accessible. Light-hole (LH) admixture means that the heavy-hole-dominated valence band states regarded in this paper get a (small) contribution from the LH band (which is usually in the range of few percent [65]). The spin-conserving and non-spin-conserving Förster coupling cases will be slightly mixed by LH admixture since the dipole moments are nonparallel in the case of LH admixture [46]. However, the opened transitions will only have a minor contribution due to the small LH admixture (below 2% [65]).

VII. CONCLUSIONS

The influence of nondiagonal Coulomb coupling on the optical properties of a coupled quantum system was studied using linear and nonlinear two-dimensional coherent spectroscopy techniques. We showed that Förster- and Dexter-type energy transfers lead to characteristic signatures in the double quantum coherence spectra, which allow us to deduce the underlying type of coupling process. The splitting of the low-energy resonance into two resonances at the hybridized level f_3 and the uncoupled resonance E_{12} is a suitable criterion to distinguish the dominant coupling mechanism by means of the relative intensities of the two resonances. It is clearly visible when spin-flipping Förster or Dexter processes take place. In the first case, the splitting is a consequence of the hybridization of all bright two excitons. In the latter case, it appears due to the coupling of bright and dark two-exciton states and the oscillator strength of the uncoupled resonance E_{12} is significantly enhanced.

Moreover, the discussion of our spectra showed that Dexter transfer processes are not limited by the optical selection rules due to the coupling to dark two excitons. Similar coupling identifying spectral patterns is expected, e.g., for bound excitons in disordered quantum wells coupled to excitons in single molecules.

ACKNOWLEDGMENT

We gratefully acknowledge financial support from the Deutsche Forschungsgemeinschaft (DFG) through SFB 787 (J.S., M.R.) and SFB 951 (A.K.).

APPENDIX: DERIVATION OF COULOMB MATRIX ELEMENTS

Starting with the general expression for the Coulomb matrix elements in Eq. (4), we first rewrite the integrals over $\boldsymbol{r}$ and $\boldsymbol{r}'$ into sums of integrals over the single unit cells (UCs):

$$\begin{aligned} V_{abcd} = \frac{e^2}{8\pi\epsilon_0\epsilon_\mathrm{r}} \sum_{\substack{i,j \\ i\neq j}}^{\mathrm{UC}} \int_{\mathrm{UC_i}} d^3r_{i1} \int_{\mathrm{UC_j}} d^3r_{j2} \\ \times \frac{\xi^*_{\lambda_a n_a}(\boldsymbol{r}_{i1})\xi^*_{\lambda_b n_b}(\boldsymbol{r}_{j2})\xi_{\lambda_d n_d}(\boldsymbol{r}_{j2})\xi_{\lambda_c n_c}(\boldsymbol{r}_{i1})}{|\boldsymbol{r}_{i1}-\boldsymbol{r}_{j2}|} \\ \times u^*_{\lambda_a n_a \sigma_a}(\boldsymbol{r}_{i1})u^*_{\lambda_b n_b \sigma_b}(\boldsymbol{r}_{j2})u_{\lambda_d n_d \sigma_d}(\boldsymbol{r}_{j2}) \\ \times u_{\lambda_c n_c \sigma_c}(\boldsymbol{r}_{i1})\,\delta_{\sigma_a\sigma_c}\delta_{\sigma_b\sigma_d}. \end{aligned} \tag{A1}$$

Here, the short-range contribution at $i=j$ has been neglected. It vanishes for Förster-type Coulomb exchange terms [66,67]. Since only the long-range contribution is taken into account in this paper, the diagonal and Dexter coupling elements are slightly underestimated. However, this limitation of the model system does not affect the general findings about the spectroscopic signatures of the different coupling mechanisms and may only slightly shift the corresponding resonances.

The vectors $\boldsymbol{r}_{kn}$ can be split into the lattice vector $\boldsymbol{R}_k$ of the kth unit cell and a small variation $\boldsymbol{s}_n$ within this cell: $\boldsymbol{r}_{kn} = \boldsymbol{R}_k + \boldsymbol{s}_n$. A three-dimensional Taylor expansion of the $\frac{1}{|\boldsymbol{r}_{i1}-\boldsymbol{r}_{j2}|}$ term up to the first order has the form [13]

$$\begin{aligned} \frac{1}{|\boldsymbol{r}_{i1}-\boldsymbol{r}_{j2}|} \simeq \frac{1}{|\boldsymbol{R}_{ij}|} - \frac{\boldsymbol{R}_{ij}}{|\boldsymbol{R}_{ij}|^3}(\boldsymbol{s}_1+\boldsymbol{s}_2) + \frac{\boldsymbol{s}_1\cdot\boldsymbol{s}_2}{|\boldsymbol{R}_{ij}|^3} \\ - \frac{3}{|\boldsymbol{R}_{ij}|^3}(\boldsymbol{s}_1\cdot\boldsymbol{R}_{ij})(\boldsymbol{s}_2\cdot\boldsymbol{R}_{ij}) \end{aligned} \tag{A2}$$

with $\boldsymbol{R}_{ij} = \boldsymbol{R}_i - \boldsymbol{R}_j$. The second term on the right-hand side of Eq. (A2) (monopole-dipole term) is neglected within the rotating-wave approximation for the quantities important for this paper. We assume that the envelope function $\xi_{\lambda n}(\boldsymbol{r})$ is constant over a unit cell: $\xi_{\lambda n}(\boldsymbol{R}_k+\boldsymbol{s}_n) \simeq \xi_{\lambda n}(\boldsymbol{R}_k)$. Furthermore, we use the invariance of the Bloch functions

under a lattice translation and their orthonormality condition $\frac{1}{V_{\rm UC}}\int_{\rm UC} d^3s_n u^*_{\lambda n\sigma}(\boldsymbol{s}_n)u_{\mu n\sigma}(\boldsymbol{s}_n)=\delta_{\lambda\mu}$. $V_{\rm UC}$ denotes the unit-cell volume. Defining the microscopic interband dipole moment for transitions between the valence and conduction band [68],

$$\boldsymbol{d}^{n\sigma}_{\lambda\mu}=\frac{1}{V_{\rm UC}}\int_{\rm UC} d^3s\, u^*_{\lambda n\sigma}(\boldsymbol{s})\, e\, \boldsymbol{s}\, u_{\mu n\sigma}(\boldsymbol{s}), \tag{A3}$$

we get the following expressions for the monopole-monopole contribution:

$$V^{\rm mono}_{abab}=\frac{e^2}{8\pi\epsilon_0\epsilon_{\rm r}}\int d^3r\int d^3r'\,\frac{\left|\xi_{\lambda_a n_a}(\boldsymbol{r})\right|^2\left|\xi_{\lambda_b n_b}(\boldsymbol{r}')\right|^2}{|\boldsymbol{r}-\boldsymbol{r}'|}\times\delta_{\lambda_a\lambda_c}\delta_{\lambda_b\lambda_d}\delta_{n_a n_c}\delta_{n_b n_d}\delta_{\sigma_a\sigma_c}\delta_{\sigma_b\sigma_d} \tag{A4}$$

for $n_a=n_c$, $n_b=n_d$ and

$$V^{\rm mono}_{abcd}=\frac{e^2}{8\pi\epsilon_0\epsilon_{\rm r}}\int d^3r\int d^3r'\times\frac{\xi^*_{\lambda_a n_a}(\boldsymbol{r})\xi^*_{\lambda_b n_b}(\boldsymbol{r}')\xi_{\lambda_b n_a}(\boldsymbol{r}')\xi_{\lambda_a n_b}(\boldsymbol{r})}{|\boldsymbol{r}-\boldsymbol{r}'|}\times\delta_{\lambda_a\lambda_c}\delta_{\lambda_b\lambda_d}\delta_{n_a n_d}\delta_{n_b n_c}\delta_{\sigma_a\sigma_c}\delta_{\sigma_b\sigma_d} \tag{A5}$$

for $n_a=n_d$, $n_b=n_c$. These two matrix elements are referred to as monopole-monopole shifts [Eq. (A4)] and Dexter terms [Eq. (A5)] throughout this work. In contrast to the diagonal monopole-monopole shifts, the Dexter terms occur as nondiagonal entries in the matrix representation of the Coulomb Hamiltonian.

The dipole-dipole terms have the form

$$V^{\rm dipole}_{abcd}=\frac{1}{8\pi\epsilon_0\epsilon_{\rm r}}\int d^3r\int d^3r'\left(\frac{\boldsymbol{d}^{n_a\sigma_a}_{\lambda_a\lambda_b}\cdot\boldsymbol{d}^{n_b\sigma_b}_{\lambda_b\lambda_a}}{|\boldsymbol{r}-\boldsymbol{r}'|^3}-3\frac{\left[\boldsymbol{d}^{n_a\sigma_a}_{\lambda_a\lambda_b}\cdot(\boldsymbol{r}-\boldsymbol{r}')\right]\left[\boldsymbol{d}^{n_b\sigma_b}_{\lambda_b\lambda_a}\cdot(\boldsymbol{r}-\boldsymbol{r}')\right]}{|\boldsymbol{r}-\boldsymbol{r}'|^5}\right)\times\xi^*_{\lambda_a n_a}(\boldsymbol{r})\xi^*_{\lambda_b n_b}(\boldsymbol{r}')\xi_{\lambda_a n_b}(\boldsymbol{r}')\xi_{\lambda_b n_a}(\boldsymbol{r})\times\delta_{\lambda_a\lambda_d}\delta_{\lambda_b\lambda_c}\delta_{n_a n_c}\delta_{n_b n_d}\delta_{\sigma_a\sigma_c}\delta_{\sigma_b\sigma_d}. \tag{A6}$$

Since the dipole moments vanish for identical band indices ($\boldsymbol{d}^{n\sigma}_{\lambda\lambda}=0$), dipole-dipole couplings represent nondiagonal elements in the Coulomb interaction matrix. The monopole-monopole and Förster terms do not require a wave-function overlap between the two nanostructures, which is expressed by the condition $n_a=n_c$ and $n_b=n_d$.

[1] A. Y. Liu, C. Zhang, J. Norman, A. Snyder, D. Lubyshev, J. M. Fastenau, A. W. K. Liu, A. C. Gossard, and J. E. Bowers, Appl. Phys. Lett. **104**, 041104 (2014).

[2] C. Santori, M. Pelton, G. Solomon, Y. Dale, and Y. Yamamoto, Phys. Rev. Lett. **86**, 1502 (2001).

[3] Q. Sun, Y. A. Wang, L. S. Li, D. Wang, T. Zhu, J. Xu, C. Yang, and Y. Li, Nat. Photonics **1**, 717 (2007).

[4] A. Nozik, Physica E (Amsterdam) **14**, 115 (2002).

[5] E. Biolatti, R. C. Iotti, P. Zanardi, and F. Rossi, Phys. Rev. Lett. **85**, 5647 (2000).

[6] K. Gawarecki, M. Pochwała, A. Grodecka-Grad, and P. Machnikowski, Phys. Rev. B **81**, 245312 (2010).

[7] N. Baer, S. Schulz, S. Schumacher, P. Gartner, G. Czycholl, and F. Jahnke, Appl. Phys. Lett. **87**, 231114 (2005).

[8] S. C. Kuhn and M. Richter, Phys. Rev. B **90**, 125308 (2014).

[9] F. V. de Sales, S. W. da Silva, J. M. R. Cruz, A. F. G. Monte, M. A. G. Soler, P. C. Morais, M. J. da Silva, and A. A. Quivy, Phys. Rev. B **70**, 235318 (2004).

[10] B. D. Gerardot, S. Strauf, M. J. A. de Dood, A. M. Bychkov, A. Badolato, K. Hennessy, E. L. Hu, D. Bouwmeester, and P. M. Petroff, Phys. Rev. Lett. **95**, 137403 (2005).

[11] S. A. Crooker, J. A. Hollingsworth, S. Tretiak, and V. I. Klimov, Phys. Rev. Lett. **89**, 186802 (2002).

[12] B. W. Lovett, J. H. Reina, A. Nazir, and G. A. D. Briggs, Phys. Rev. B **68**, 205319 (2003).

[13] J. Danckwerts, K. J. Ahn, J. Förstner, and A. Knorr, Phys. Rev. B **73**, 165318 (2006).

[14] M. Richter, K. J. Ahn, A. Knorr, A. Schliwa, D. Bimberg, M. E.-A. Madjet, and T. Renger, Phys. Status Solidi B **243**, 2302 (2006).

[15] A. Carmele, A. Knorr, and M. Richter, Phys. Rev. B **79**, 035316 (2009).

[16] D. L. Dexter, J. Chem. Phys. **21**, 836 (1953).

[17] G. D. Scholes and D. L. Andrews, Phys. Rev. B **72**, 125331 (2005).

[18] A. Imamoglu, D. D. Awschalom, G. Burkard, D. P. DiVincenzo, D. Loss, M. Sherwin, and A. Small, Phys. Rev. Lett. **83**, 4204 (1999).

[19] J. M. Kikkawa and D. D. Awschalom, Phys. Rev. Lett. **80**, 4313 (1998).

[20] T. Förster, Ann. Phys. **437**, 55 (1948).

[21] V. M. Agranovich and M. D. Galanin, in *Electronic Excitation Energy Transfer in Condensed Matter*, edited by V. M. Agranovich and A. A. Maradudin (North-Holland, Amsterdam, 1982).

[22] G. D. Scholes, Annu. Rev. Phys. Chem. **54**, 57 (2003).

[23] S. Mukamel, Annu. Rev. Phys. Chem. **51**, 691 (2000).

[24] P. Tian, D. Keusters, Y. Suzaki, and W. S. Warren, Science **300**, 1553 (2003).

[25] V. M. Axt and T. Kuhn, Rep. Prog. Phys. **67**, 433 (2004).

[26] I. Kuznetsova, P. Thomas, T. Meier, T. Zhang, X. Li, R. Mirin, and S. Cundiff, Solid State Commun. **142**, 154 (2007).

[27] I. Kuznetsova, T. Meier, S. T. Cundiff, and P. Thomas, Phys. Rev. B **76**, 153301 (2007).

[28] D. Karaiskaj, A. D. Bristow, L. Yang, X. Dai, R. P. Mirin, S. Mukamel, and S. T. Cundiff, Phys. Rev. Lett. **104**, 117401 (2010).

[29] T. U.-K. Dang, C. Weber, S. Eiser, A. Knorr, and M. Richter, Phys. Rev. B **86**, 155306 (2012).

[30] S. Mukamel, *Principles of Nonlinear Optical Spectroscopy* (Oxford University Press, New York, 1995).

[31] L. Yang and S. Mukamel, Phys. Rev. Lett. **100**, 057402 (2008).

[32] D. Abramavicius, B. Palmieri, D. V. Voronine, F. Sanda, and S. Mukamel, Chem. Rev. **109**, 2350 (2009).

[33] H. Haug and S. W. Koch, *Quantum Theory of the Optical and Electronic Properties of Semiconductors* (World Scientific, Singapore, 2004).

[34] P. Y. Yu and M. Cardona, *Fundamentals of Semiconductors* (Springer, Berlin, 2005).
[35] S. Sauvage, P. Boucaud, J. M. Gerard, and V. Thierry-Mieg, Phys. Rev. B **58**, 10562 (1998).
[36] L. R. Wilson, D. J. Mowbray, M. S. Skolnick, M. Morifuji, M. J. Steer, I. A. Larkin, and M. Hopkinson, Phys. Rev. B **57**, R2073 (1998).
[37] A. Grodecka, P. Machnikowski, and J. Förstner, Phys. Rev. B **78**, 085302 (2008).
[38] B. Fornberg and D. M. Sloan, Acta Numerica **3**, 203 (1994).
[39] P. Machnikowski and E. Rozbicki, Phys. Status Solidi B **246**, 320 (2009).
[40] L. R. C. Fonseca, J. L. Jimenez, J. P. Leburton, and R. M. Martin, Phys. Rev. B **57**, 4017 (1998).
[41] E. Stock, M.-R. Dachner, T. Warming, A. Schliwa, A. Lochmann, A. Hoffmann, A. I. Toropov, A. K. Bakarov, I. A. Derebezov, M. Richter, V. A. Haisler, A. Knorr, and D. Bimberg, Phys. Rev. B **83**, 041304 (2011).
[42] I. A. Ostapenko, G. Hönig, S. Rodt, A. Schliwa, A. Hoffmann, D. Bimberg, M.-R. Dachner, M. Richter, A. Knorr, S. Kako, and Y. Arakawa, Phys. Rev. B **85**, 081303 (2012).
[43] C. Curutchet, A. Franceschetti, A. Zunger, and G. D. Scholes, J. Phys. Chem. C **112**, 13336 (2008).
[44] A. O. Govorov, Phys. Rev. B **68**, 075315 (2003).
[45] A. O. Govorov, Phys. Rev. B **71**, 155323 (2005).
[46] A. Sitek and P. Machnikowski, Phys. Rev. B **86**, 205315 (2012).
[47] D. P. Craig and T. Thirunamachandran, *Molecular Quantum Electrodynamics: An Introduction to Radiation Molecule Interactions* (Dover, Mineola, NY, 2003).
[48] F. Schlosser, A. Knorr, S. Mukamel, and M. Richter, New J. Phys. **15**, 025004 (2013).
[49] P. Borri, W. Langbein, S. Schneider, U. Woggon, R. L. Sellin, D. Ouyang, and D. Bimberg, Phys. Rev. Lett. **87**, 157401 (2001).
[50] B. P. Fingerhut, M. Richter, J.-W. Luo, A. Zunger, and S. Mukamel, Ann. Phys. **525**, 31 (2013).
[51] F. Meier and B. P. Zakharchenya, *Optical Orientation* (North-Holland, Amsterdam, 1984).
[52] G. D. Scholes, J. Chem. Phys. **121**, 10104 (2004).
[53] B. Hanewinkel, A. Knorr, P. Thomas, and S. W. Koch, Phys. Rev. B **55**, 13715 (1997).
[54] P. G. Eliseev, H. Li, A. Stintz, G. T. Liu, T. C. Newell, K. J. Malloy, and L. F. Lester, Appl. Phys. Lett. **77**, 262 (2000).
[55] J. Gomis-Bresco, S. Dommers, V. V. Temnov, U. Woggon, M. Laemmlin, D. Bimberg, E. Malic, M. Richter, E. Schöll, and A. Knorr, Phys. Rev. Lett. **101**, 256803 (2008).
[56] J. R. Guest, T. H. Stievater, X. Li, J. Cheng, D. G. Steel, D. Gammon, D. S. Katzer, D. Park, C. Ell, A. Thränhardt, G. Khitrova, and H. M. Gibbs, Phys. Rev. B **65**, 241310 (2002).
[57] M. Aeschlimann, T. Brixner, A. Fischer, C. Kramer, P. Melchior, W. Pfeiffer, C. Schneider, C. Strüber, P. Tuchscherer, and D. V. Voronine, Science **333**, 1723 (2011).
[58] T. Brixner, F. J. García de Abajo, J. Schneider, and W. Pfeiffer, Phys. Rev. Lett. **95**, 093901 (2005).
[59] A. M. Weiner, Rev. Sci. Instrum. **71**, 1929 (2000).
[60] H. D. Robinson and B. B. Goldberg, Phys. Rev. B **61**, R5086 (2000).
[61] J. F. Kruiger, C. P. van der Vegte, and T. L. C. Jansen, J. Chem. Phys. **142**, 054201 (2015).
[62] W. Langbein and B. Patton, J. Phys.: Condens. Matter **19**, 295203 (2007).
[63] G. Moody, M. E. Siemens, A. D. Bristow, X. Dai, D. Karaiskaj, A. S. Bracker, D. Gammon, and S. T. Cundiff, Phys. Rev. B **83**, 115324 (2011).
[64] A. V. Koudinov, I. A. Akimov, Y. G. Kusrayev, and F. Henneberger, Phys. Rev. B **70**, 241305 (2004).
[65] K. Gawarecki and P. Machnikowski, Phys. Rev. B **85**, 041305 (2012).
[66] P. Kowalski, L. Marcinowski, and P. Machnikowski, Phys. Rev. B **87**, 075309 (2013).
[67] E. Kadantsev and P. Hawrylak, Phys. Rev. B **81**, 045311 (2010).
[68] C. Weber, M. Richter, S. Ritter, and A. Knorr, in *Semiconductor Nanostructures*, NanoScience and Technology, edited by D. Bimberg (Springer, Berlin, 2008), Chap. 9, pp. 189–210.